QUANTUM INFORMATION

Observation of an environmentally insensitive solid-state spin defect in diamond

Brendon C. Rose[1]*, Ding Huang[1]*, Zi-Huai Zhang[1], Paul Stevenson[1],
Alexei M. Tyryshkin[1], Sorawis Sangtawesin[1], Srikanth Srinivasan[1], Lorne Loudin[2],
Matthew L. Markham[3], Andrew M. Edmonds[3], Daniel J. Twitchen[3],
Stephen A. Lyon[1], Nathalie P. de Leon[1]†

Engineering coherent systems is a central goal of quantum science. Color centers in diamond are a promising approach, with the potential to combine the coherence of atoms with the scalability of a solid-state platform. We report a color center that shows insensitivity to environmental decoherence caused by phonons and electric field noise: the neutral charge state of silicon vacancy (SiV^0). Through careful materials engineering, we achieved >80% conversion of implanted silicon to SiV^0. SiV^0 exhibits spin-lattice relaxation times approaching 1 minute and coherence times approaching 1 second. Its optical properties are very favorable, with ~90% of its emission into the zero-phonon line and near–transform-limited optical linewidths. These combined properties make SiV^0 a promising defect for quantum network applications.

P oint defects in diamond known as color centers are a promising physical platform for quantum science and quantum information processing. As atomlike systems, they can exhibit excellent spin coherence and can be manipulated with light. As solid-state defects, they can be placed together at high densities and incorporated into scalable devices. Diamond is an unusually excellent host: it has a large bandgap, can be synthesized with impurity concentrations below the parts-per-billion scale, and can be isotopically purified to eliminate magnetic noise from nuclear spins (*1*). The well-studied negatively charged nitrogen vacancy (NV⁻) center exhibits long electron spin coherence times even at room temperature and has been used to demonstrate basic building blocks of quantum networks, including spin-photon entanglement (*2*), entanglement with nearby nuclear spins to form quantum registers (*3, 4*), remote entanglement of two NV⁻ centers (*5, 6*), quantum teleportation (*7*), and entanglement distillation (*8*). Despite these experimental achievements, the NV⁻ center suffers from a low spin-photon entanglement generation rate that is limited by its optical properties. In particular, only a small fraction of NV⁻ emission is at the zero-phonon line (ZPL), which can be parameterized by its Debye-Waller factor of 0.03 (*9*). Furthermore, NV⁻ exhibits a large static inhomogeneous linewidth (*10*) and substantial spectral diffusion (*11*), particularly when placed near surfaces (*12*), which results from a large

difference in the permanent electric dipole moment between the ground and excited states. These optical properties severely limit the utility of NV⁻ centers for future scalable quantum networks.

Recently, the negatively charged silicon vacancy (SiV⁻) center has been demonstrated to have more favorable optical properties. The SiV⁻ center exhibits a large Debye-Waller factor of 0.7 (*13*), narrow inhomogeneous linewidth, and single-center linewidths with minimal spectral diffusion (*14, 15*). These narrow linewidths arise from its D_{3d} molecular configuration, as inversion symmetry guarantees a vanishing permanent electric dipole moment, making the optical transition frequency insensitive to electric field noise. These properties have enabled demonstrations of two-photon interference from distinct emitters (*15*) and strong atom-photon interactions in a nanophotonic cavity (*16*). However, orbital relaxation through electron-phonon coupling limits the SiV⁻ electron spin coherence time (T_2) to 38 ns at liquid helium temperature, 4.5 K (*14*). This results from its imbalanced electronic spin configuration, with total spin $S = \frac{1}{2}$ in doubly degenerate orbitals, making SiV⁻ prone to phonon-mediated, dynamic Jahn-Teller–like orbital relaxation (*17*).

These promising demonstrations motivated us to search for other color centers in diamond that combine the attractive optical properties of SiV⁻ with the long spin coherence time of NV⁻. A natural approach is to tune the Fermi level of diamond to stabilize a different charge state of the silicon vacancy center for the purpose of accessing a different spin configuration (*18, 19*) while preserving inversion symmetry. There is some evidence that different charge states of SiV have been observed in uncontrolled samples (*20–22*). Previous work has helped to establish

a connection between photoluminescence (PL) at 946 nm and the KUL1 defect observed in electron spin resonance (ESR) measurements (*S* = 1, zero field splitting *D* = 942 MHz) (*20–22*) by correlating the PL intensity with ESR transitions across several samples. Charge transfer experiments from SiV⁻ suggest that the KUL1 center is the neutral charge state of the same center, SiV^0 (*21*).

Here we report the stabilization and characterization of SiV^0 by deliberate engineering of the diamond host. We accomplish this by careful control over the concentration of co-occurring defects in the diamond to pin the Fermi level such that the neutral charge state has the lowest formation energy (*23*). Fermi level engineering in diamond is challenging, as it relies on charge compensation between deep defects (*24*) and thus requires meticulous characterization and control of all defects, including heteroatoms, molecular point defects, lattice damage, and extended defects. Furthermore, the presence of other defects in the lattice can complicate characterization of fundamental properties of color centers, and we show that through careful materials engineering, we are able to uncover highly coherent optical and spin properties of SiV^0.

To disentangle the contributions of different defects, we first studied a modulation-doped diamond (the layered sample) that allowed a wide range of relative co-defect concentrations to be accessed in a single sample (Fig. 1B, left). This diamond was grown by microwave plasma–enhanced chemical vapor deposition on a (100) high-pressure, high-temperature substrate, and both the boron and silicon concentrations were ramped throughout the growth (*25*). The boron precursor was shut off to create a 200-μm low-boron {[B] < 35 parts per billion (ppb)} region in the middle of the sample. In this layered sample, we observed emission at 946 nm in bulk PL (Fig. 1A) as well as the KUL1 center in bulk X-band (9.7 GHz) ESR (Fig. 1C). Specifically, we observed four sets of peaks with the external magnetic field aligned along a <111> axis, consistent with the two inequivalent orientations with splittings that correspond to S = 1, D = 942 MHz. Furthermore, the hyperfine structure of a single peak is consistent with prior measurements (*20*) (Fig. 1C, inset), and the single pair of ¹³C hyperfine peaks is indicative of the inversion symmetry of the center. From the Hahn echo intensities compared to the known Si concentration in the sample, we estimated that only a small fraction of the Si exists as SiV^0 (*25*).

The apparent optical and spin properties of SiV^0 in the layered sample were complicated by heterogeneity and the presence of co-defects. The PL spectrum shows broad emission to the red of 946 nm, as well as three peaks at 952, 975, and 985 nm, which may be associated with other defects (Fig. 1A). Time-resolved pulsed ESR measurements of this sample exhibit multiexponential decays for both T_1 (spin relaxation time) and T_2 (fig. S8), most likely because of dipolar interactions between SiV^0 centers and interactions with uncontrolled co-defects.

[1]Department of Electrical Engineering, Princeton University, Princeton, NJ 08544, USA. [2]Gemological Institute of America, New York, NY 10036, USA. [3]Element Six, Harwell OX11 0QR, UK.
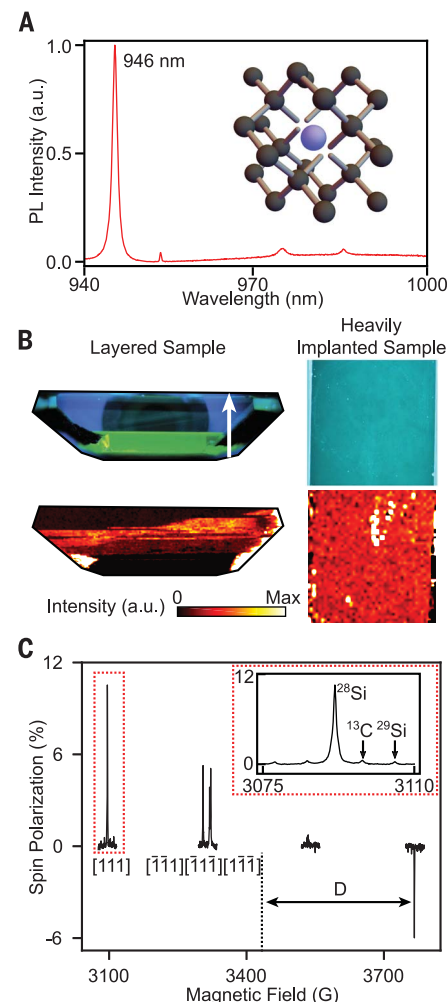*These authors contributed equally to this work.
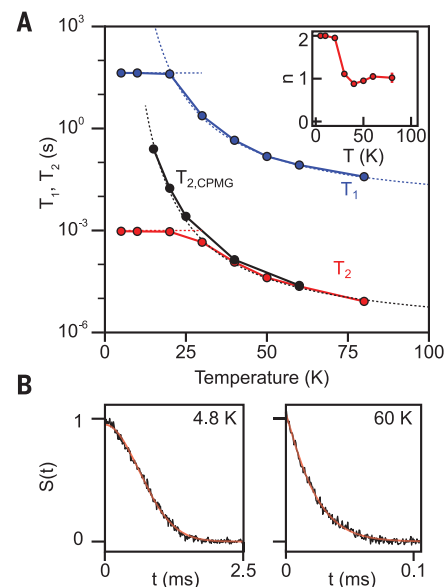†Corresponding author. Email: npdeleon@princeton.edu

Fig. 1. Stabilizing SiV⁰ centers in diamond.
(**A**) Bulk PL spectrum of SiV⁰ at 77 K showing a ZPL at 946 nm. (Inset) Ball-and-stick model of the SiV center in diamond. The interstitial Si atom (blue sphere) and split vacancy are aligned along the [111] direction in the diamond lattice. a.u., arbitrary units. (**B**) PL with above-bandgap excitation (top) and PL map of emission at 946 nm using 780-nm excitation (bottom) for the two samples under investigation. The above-bandgap PL images are color-calibrated DiamondView images that show all luminescence with wavelengths above 225 nm (*25*). The color bar for the 946-nm emission shows intensity scaled to enhance contrast. Layered diamond (left) is grown by plasma-enhanced chemical vapor deposition with B and Si concentrations varied during the growth. The growth direction is indicated with a white arrow. PL at 946 nm is localized to a few growth bands. The heavily implanted sample (right) with uniform boron doping and implanted Si has nearly uniform PL at 946 nm. Saturated intensity (white) corresponds to background and interference arising from the graphitic edges of the sample or broadband PL from the metallic cold finger. (**C**) Pulsed ESR spectrum at 9.7 GHz with magnetic field **B** parallel to [111], identifying KUL1 ($S = 1$, $D = 942$ MHz or 336 G) in the heavily implanted sample under green laser excitation for optically enhanced spin polarization. The resonant field for $S = \frac{1}{2}$ and a free electron g-factor is indicated as a dashed vertical line near the center of the plot. Four sets of peaks correspond to the two inequivalent orientations: one aligned with the field and three equivalent orientations at 109.5° from the field. The outer peaks at low and high magnetic field correspond to the orientation aligned with the magnetic field, [111]. The two sets of inner peaks closer to the vertical dashed line (marking the resonant field for a free electron g-factor) correspond to the other three orientations, and a slight misalignment of the field from [111] splits the peaks into three resolvable lines. The optical spin polarization has the opposite sign with respect to thermal polarization, so the two sets of higher field lines are diminished by the combination of mechanisms. Optical spin polarization is also less efficient in the presence of strong off-axis magnetic fields, so the inner peaks have lower intensity than the outer peaks. (Inset) Hyperfine structure of an individual transition shows ¹³C and ²⁹Si peaks. The same pulsed ESR spectrum is observed in both the layered and heavily implanted samples. The red boxes denote the region of the plot that is contained in the inset.

Fig. 2. Spin relaxation time (T₁) and coherence time (T₂) measurements.
(**A**) Temperature dependence of T_1 (blue symbols), T_2 (red symbols), and $T_{2,CPMG}$ (black symbols) for SiV⁰ measured on the $m_s = 0 \leftrightarrow +1$ transition of the orientation aligned with the magnetic field. Below 20 K, both T_1 and T_2 are independent of temperature, with $T_1 = 43 \pm 2$ s and $T_2 = 0.954 \pm 0.025$ ms. Above 20 K, both T_1 and T_2 show a temperature dependence consistent with an Orbach process with an activation energy of 16.8 meV (dashed blue and black lines are fits). Dynamical decoupling with CPMG (black symbols) extends the coherence time to $T_{2,CPMG} = 255 \pm 20$ ms at 15 K. (Inset) Temperature dependence of the exponential stretching factor, n, in the T_2 decay showing a step in the stretching factor at 20 K. (**B**) Selected Hahn echo decay curves illustrating $n = 2$ in the low-temperature regime (4.8 K) and $n = 1$ in the high-temperature regime (60 K).

We definitively verified the connection between the ESR and PL transitions by scanning a laser across the optical transition while measuring the polarization of the $m_s = 0 \leftrightarrow +1$ spin transition (m_s, magnetic component of the spin quantum number) at cryogenic temperatures (4.8 K) (fig. S10). We observed strong changes in bulk spin polarization as we scanned the laser across 946 nm, showing that the optical and ESR transitions arise from the same defect. Armed with this assignment, spatially resolved PL mapping reveals that 946-nm emission is localized in specific growth bands in the layered sample (Fig. 1B, bottom left), suggesting that SiV⁰ may form more efficiently in certain growth environments. Correlating these regions with spatially resolved secondary ion mass spectrometry indi-

cates that SiV⁰ forms in regions with [B] = 1 to 3 parts per million (ppm), [Si] = 400 ppb, and [N] below the detection limit of the technique, estimated to be ~1 ppb from prior characterization of growth conditions (fig. S4). Using this information, we prepared a homogeneous, heavily implanted sample with a uniform distribution of SiV⁰ by implanting ²⁸Si into high-purity diamond with [B] = 1 ppm and [N] < 5 ppb. A range of implantation energies (table S2) was used to generate a sample with a signal large enough for bulk ESR and density low enough to avoid dipolar interactions between pairs of SiV⁰ (<50 ppb). Before ion implantation, we etched 5 to 10 μm of diamond to remove subsurface damage from polishing (*12*). After ion implantation, thermal annealing at 800° and

1200°C forms SiV⁰ and repairs implantation-induced lattice damage (*12*). Both steps are critical for suppressing environmental noise and Fermi level pinning from lattice damage. In contrast to the layered sample, PL mapping of this heavily implanted sample shows a homogeneous distribution of 946-nm emission (Fig. 1B, bottom right), and ESR spin counting indicates a conversion efficiency from implanted ²⁸Si to SiV⁰ of >80% (fig. S7).

The heavily implanted sample exhibits markedly different behavior in time-resolved ESR compared with the layered sample. Both the electron spin coherence and relaxation times show single exponential behavior, indicating that the SiV⁰ environment is homogeneous (Fig. 2B). Below 20 K, the electron spin coherence time measured using a Hahn echo sequence is $T_2 = 0.954 \pm 0.025$ ms, and the spin relaxation time is measured to be $T_1 = 43 \pm 2$ s (Fig. 2A) (*26*). Both are
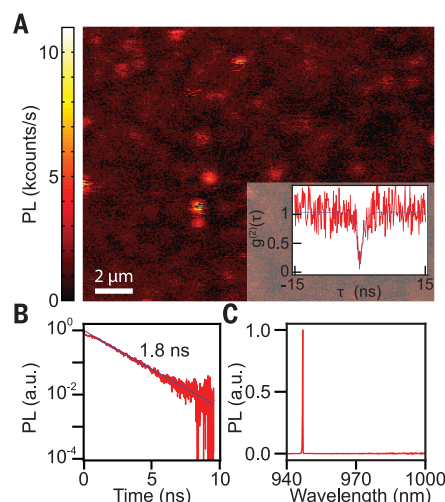
Fig. 3. Optical properties of SiV⁰. (**A**) Scanning confocal PL image of SiV⁰ centers in the lightly implanted sample. (Inset) Second-order correlation function $g^{(2)}(\tau)$ (τ, time delay between photon arrivals) of the PL from a single spot with $g^{(2)}(0) < 0.5$, indicating that the PL originates primarily from a single emitter. (**B**) Time-dependent PL measured using a pulsed laser at 780 nm. The single exponential fit indicates an excited-state lifetime of 1.8 ns at 4 K. (**C**) PL spectrum of a single SiV⁰ center. The emission is collected into a spectrometer-limited peak on a charge-coupled device spectrometer (0.1-nm resolution), and there is no observable phonon sideband out to 1000 nm.

independent of temperature. This spin coherence time is more than four orders of magnitude longer than the $T_2 = 35$ ns reported for SiV⁻ at 4.5 K (14), which is limited by an orbital $T_1 = 38$ ns (14). The temperature independence of the spin relaxation in SiV⁰ is similar to previous observations of NV⁻ ensembles (27). The mechanism limiting T_1 at low temperatures remains unknown, but the direct (single-phonon) relaxation process can be excluded because it would have a T^{-1} dependence.

The decoherence mechanism at low temperature can be inferred by the stretching factor, n, extracted from the Hahn echo decay signal $S(t)$ (Fig. 2B) by fitting the data to a stretched exponential, $S(t) = A \cdot \exp[-(t/T_2)^n]$ (t, time). The stretching factor $n = 2$ (Fig. 2A, inset) indicates that the coherence time is dominated by slowly-varying noise, which likely arises from the 1.1% natural abundance of ¹³C nuclei in this sample (28), similar to what is observed for NV⁻ centers (29, 30). Dynamical decoupling with the Carr-Purcell-Meiboom-Gill (CPMG) sequence (31) refocuses decoherence from ¹³C spectral diffusion, extending the coherence time to $T_{2,\text{CPMG}} = 255 \pm 20$ ms at 15 K (Fig. 2A, black symbols), limited in our experiments by pulse error accumulation.

At temperatures above 20 K, both T_1 and T_2 rapidly decrease with increasing temperature.
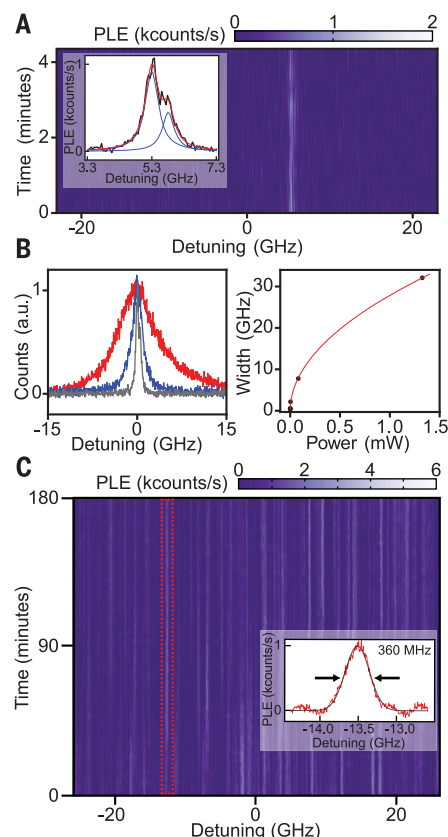
Fig. 4. PLE spectroscopy. (**A**) PLE scan on a single center in the lightly implanted sample, showing a single line that is spectrally stable over ~4 min of interrogation. (Inset) PLE integrated over all the scans (black), with the baseline subtracted (25). The fit (red) represents the sum of two overlapping Lorentzians (blue) with individual widths [full width at half maximum (FWHM)] of 450 and 499 MHz for the left and right peaks, respectively. (**B**) (Left) PLE scans of the line from (A) at different excitation powers: 150 nW (gray), 3.2 μW (blue), and 81 μW (red), resulting in linewidths of 450 MHz, 2.2 GHz, and 7.8 GHz, respectively. (Right) The linewidth as a function of excitation power P, showing the power broadening in detail. The red line corresponds to $\Gamma(P) = G\sqrt{1 + P/P_0}$ where Γ is the FWHM of the optical transition, $G = 0.255$ GHz, and $P_0 = 78$ nW. (**C**) Ensemble PLE in the heavily implanted sample. The scan reveals many lines that are stable across 80 iterations spanning a 3-hour period. (Inset) Gaussian fit to a single isolated peak, integrated over all of the scans, with the baseline subtracted, showing a FWHM of 360 MHz.

The temperature dependence of the spin relaxation is consistent with an Orbach spin relaxation process, $T_1 \propto \exp(-E_a/k_B T)$, with an activation energy $E_a = 16.8$ meV (k_B, Boltzmann constant; T, temperature). Both T_2 and $T_{2,\text{CPMG}}$ exhibit a similar temperature dependence to the spin relaxation but scaled by a constant factor of

4100, indicating that the decay in T_2 with temperature is related to the same Orbach process.

We then turned our attention to optical characterization of SiV⁰ at low temperature. To optically examine single SiV⁰ centers, we implanted silicon ions at a dose of 10^9 cm⁻² into a lightly boron-doped diamond, followed by high-temperature annealing to form SiV⁰ (the lightly implanted sample). A confocal scan at 5 K with off-resonant excitation (905 nm, 28 mW) and detection at wavelengths longer than 930 nm shows isolated and diffraction-limited PL spots with a peak intensity >10 kilocounts per second (kcounts/s) (Fig. 3A). Second-order photon correlation statistics from an isolated spot show a dip at zero-time delay, $g^{(2)}(0) = 0.126 \pm 0.037$ (Fig. 3A, inset), confirming that these spots arise from single-photon emitters. A power dependence of the PL intensity reveals that the saturated count rate is 37.5 kcounts/s (fig. S12A). Taking the saturated photon count rate and accounting for the low quantum efficiency of the detector (22%), transmission through a beamsplitter (55%), and transmission through the high–numerical aperture and fiber-coupling objectives (74 and 85%, respectively) in this wavelength range, we estimate that this corresponds to a photon emission rate of ~500,000 photons/s (25). Additionally, we note that bright emitters have a broader inhomogeneous distribution (>20 nm) than the bulk PL linewidth of <1 nm measured in the heavily implanted sample (fig. S16). This distribution in wavelength is most likely a result of surface-related strain and is consistent with recent measurements of SiV⁻ where inhomogeneous distributions of ~20 nm have been observed in nanodiamonds (32, 33).

In contrast to bulk PL in the layered sample, the emission spectra of single centers in the implanted samples exhibit narrow, spectrometer-limited peaks (0.1-nm resolution) with no discernible phonon sideband (Fig. 3C). We estimate a lower bound on the Debye-Waller factor by comparing the intensity at the ZPL with the integrated intensity from 947 to 1000 nm, which includes background and noise. Using this comparison, we estimate that 90 ± 10% of the emission is in the ZPL (25). This is counter to previous estimates of the Debye-Waller factor of SiV⁰, which were complicated by the presence of uncontrolled co-defects in this wavelength range (21).

We thoroughly investigated the optical transitions of SiV⁰ by using photoluminescence excitation (PLE) spectroscopy (Fig. 4), in which a narrow-linewidth laser (<200 kHz) is scanned across the SiV⁰ ZPL while emission is measured at wavelengths above 960 nm. Despite the absence of a clear phonon sideband above the noise in the PL spectrum (Fig. 3C), we observed a small but measurable increase in photon counts (1 to 5 kcounts/s) at wavelengths above 960 nm with resonant excitation at 946 nm. PLE scans of a single center in the lightly implanted sample reveal two overlapping lines with linewidths 450 and 499 MHz that are observed to be spectrally stable over minutes of investigation (Fig. 4A).

These linewidths are five times as large as the transform-limited linewidth of 88 MHz determined by the bulk PL excited-state lifetime of 1.8 ns (Fig. 3B). At higher laser excitation powers, the PLE linewidths increase (Fig. 4B), and the saturation power extracted from the fit is 78 nW. This is somewhat larger than the predicted value of 10 nW, with the discrepancy likely attributable to mismatch between the laser and dipole polarizations and a finite decay probability into other ground states (*25*).

A PLE scan of the heavily implanted sample reveals many narrow lines with linewidths ranging from 250 to 500 MHz (Fig. 4C). Repeated scans over a 3-hour period show that these lines are completely stable in frequency, showing no measurable sign of spectral diffusion. This indicates that stable, near–transform-limited optical lines are a robust property of SiV^0, in stark contrast to implanted NV$^-$ centers, which exhibit optical linewidths 10 to 100 times their natural linewidth (*12*).

Building on this demonstration of a color center in diamond with long spin coherence time and spectrally stable optical transitions, the high-purity, homogeneous samples discussed here will allow for detailed characterization of the fine structure and selection rules of the optical transitions, accurate determination of quantum efficiency, and further characterization of the ground-state spin. Ongoing investigations include studies of the origin of the Orbach process above 20 K (*34*) and schemes for dynamic stabilization of the charge state during optical excitation. We achieved up to 44% bulk spin polarization by using resonant optical excitation (fig. S10), suggesting the existence of spin-conserving and spin-pumping optical transitions, which are key ingredients for quantum networks. In addition, SiV^0 contains an intrinsic longer-lived quantum memory in the form of the ^{29}Si nuclear spin within the defect. Preliminarily, we measured nuclear spin coherence times of $T_{2n} = 0.45 \pm 0.03$ s in a ^{29}Si-enriched sample (fig. S9), and future work will explore the limits of this coherence in samples with lower spin density.

Furthermore, SiV^0 is a particularly attractive candidate for implementing a single-atom quantum memory in a quantum network through integration with quantum nanophotonic devices. The high conversion efficiency for implanted centers is advantageous for nanoscale patterning and registration (*35*). The emission wavelength at 946 nm is compatible with heterogeneously integrated GaAs photonics (*36*), and efficient, low-noise frequency conversion to telecommunications wavelengths (1550 nm) at the single-photon level using three-wave mixing has already been demonstrated at 980 nm (*37*).

Our methods for Fermi level engineering using careful control over co-occurring defects can be broadly applied to alter the charge state of other known color centers, such as the germanium (*38*) and tin (*39*) vacancy centers, as well as for discovery of entirely new color centers in diamond.

REFERENCES AND NOTES

1. G. Balasubramanian et al., *Nat. Mater.* **8**, 383–387 (2009).
2. E. Togan et al., *Nature* **466**, 730–734 (2010).
3. P. C. Maurer et al., *Science* **336**, 1283–1286 (2012).
4. F. Dolde et al., *Nat. Phys.* **9**, 139–143 (2013).
5. H. Bernien et al., *Nature* **497**, 86–90 (2013).
6. B. Hensen et al., *Nature* **526**, 682–686 (2015).
7. W. Pfaff et al., *Science* **345**, 532–535 (2014).
8. N. Kalb et al., *Science* **356**, 928–932 (2017).
9. P. E. Barclay, K.-M. C. Fu, C. Santori, A. Faraon, R. G. Beausoleil, *Phys. Rev. X* **1**, 011007 (2011).
10. P. Olivero et al., *New J. Phys.* **15**, 043027 (2013).
11. J. Wolters, N. Sadzak, A. W. Schell, T. Schröder, O. Benson, *Phys. Rev. Lett.* **110**, 027401 (2013).
12. Y. Chu et al., *Nano Lett.* **14**, 1982–1986 (2014).
13. A. Dietrich et al., *New J. Phys.* **16**, 113019 (2014).
14. L. J. Rogers et al., *Phys. Rev. Lett.* **113**, 263602 (2014).
15. A. Sipahigil et al., *Phys. Rev. Lett.* **113**, 113602 (2014).
16. A. Sipahigil et al., *Science* **354**, 847–850 (2016).
17. K. D. Jahnke et al., *New J. Phys.* **17**, 043011 (2015).
18. A. Gali, M. Fyta, E. Kaxiras, *Phys. Rev. B* **77**, 155206 (2008).
19. J. R. Maze et al., *New J. Phys.* **13**, 025025 (2011).
20. A. M. Edmonds, M. E. Newton, P. M. Martineau, D. J. Twitchen, S. D. Williams, *Phys. Rev. B* **77**, 245205 (2008).
21. U. F. S. D'Haenens-Johansson et al., *Phys. Rev. B* **84**, 245208 (2011).
22. J. P. Goss, R. Jones, S. J. Breuer, P. R. Briddon, S. Öberg, *Phys. Rev. Lett.* **77**, 3041–3044 (1996).
23. A. Gali, J. R. Maze, *Phys. Rev. B* **88**, 235205 (2013).
24. A. T. Collins, *J. Phys. Condens. Matter* **14**, 3743–3750 (2002).
25. See supplementary materials.
26. During the preparation of this manuscript, a related study on SiV^0 spin relaxation and optical spin polarization was published (*40*).
27. A. Jarmola, V. M. Acosta, K. Jensen, S. Chemerisov, D. Budker, *Phys. Rev. Lett.* **108**, 197601 (2012).
28. W. B. Mims, K. Nassau, J. D. McGee, *Phys. Rev.* **123**, 2059–2069 (1961).
29. P. L. Stanwix et al., *Phys. Rev. B* **82**, 201201(R) (2010).
30. B. C. Rose, C. D. Weis, A. M. Tyryshkin, T. Schenkel, S. A. Lyon, *Diamond Related Materials* **72**, 32–40 (2017).
31. S. Meiboom, D. Gill, *Rev. Sci. Instrum.* **29**, 688–691 (1958).
32. E. Neu et al., *New J. Phys.* **13**, 025012 (2011).
33. E. Neu, M. Fischer, S. Gsell, M. Schreck, C. Becher, *Phys. Rev. B* **84**, 205211 (2011).
34. B. C. Rose et al., arXiv:1710.03196 [quant-ph] (9 October 2017).
35. D. M. Toyli, C. D. Weis, G. D. Fuchs, T. Schenkel, D. D. Awschalom, *Nano Lett.* **10**, 3168–3172 (2010).
36. D. Englund et al., *Phys. Rev. Lett.* **95**, 013904 (2005).
37. Q. Li, M. Davanco, K. Srinivasan, *Nat. Photonics* **10**, 406–414 (2016).
38. T. Iwasaki et al., *Sci. Rep.* **5**, 12882 (2015).
39. T. Iwasaki et al., *Phys. Rev. Lett.* **119**, 253601 (2017).
40. B. L. Green et al., *Phys. Rev. Lett.* **119**, 096402 (2017).
41. B. C. Rose et al., Replication Data for: Observation of an environmentally insensitive solid state spin defect in diamond, version 1, Harvard Dataverse (2018) https://doi.org/10.7910/DVN/FUQDFQ.

Science

Observation of an environmentally insensitive solid-state spin defect in diamond

Brendon C. Rose, Ding Huang, Zi-Huai Zhang, Paul Stevenson, Alexei M. Tyryshkin, Sorawis Sangtawesin, Srikanth Srinivasan, Lorne Loudin, Matthew L. Markham, Andrew M. Edmonds, Daniel J. Twitchen, Stephen A. Lyon and Nathalie P. de Leon

In search of the right diamond defect
Certain defects in diamond are among the most promising physical implementations of qubits, the building blocks of quantum computers. However, identifying a defect with balanced properties is tricky: Nitrogen vacancy centers have a long lifetime but comparatively poor optical properties, whereas negatively charged silicon vacancy centers have the opposite characteristics. Rose *et al.* used careful materials engineering to stabilize the neutral charge state of silicon vacancy centers and found that they combine long coherence times with excellent optical properties.
Science, this issue p. 60

ARTICLE TOOLS	http://science.sciencemag.org/content/361/6397/60
SUPPLEMENTARY MATERIALS	http://science.sciencemag.org/content/suppl/2018/07/03/361.6397.60.DC1
REFERENCES	This article cites 41 articles, 4 of which you can access for free http://science.sciencemag.org/content/361/6397/60#BIBL
PERMISSIONS	http://www.sciencemag.org/help/reprints-and-permissions

Use of this article is subject to the Terms of Service